

Carbon Nanotube Reinforced CdSe Inverse Opal with Crack-Free Structure and High Conductivity for Photovoltaic Applications

Xue-Li Zheng, Wen-Jing Qin, Tao Ling, Cao-Feng Pan, and Xi-Wen Du*

Inverse opal is a well-known three-dimensional structure with highly uniform and periodic pores surrounded by solid walls.^[1–4] It has shown great potential in many applications, such as catalysis,^[5,6] energy conversion,^[7–11] energy storage,^[12,13] and tissue engineering,^[14,15] because the connected pores provide a prodigious surface area for adsorption–desorption,^[16] ion-exchange,^[17] and charge separation,^[18] while the periodic architecture was demonstrated to enhance light harvesting efficiency remarkably by photonic or backscattering effect.^[19]

In principle, the fabrication of inverse opal structures involves two steps.^[20–22] First, template spheres and nanoparticles were assembled on a substrate via a co-deposition process, leading to a compact film with periodic distribution of template. Second, the template spheres were removed by annealing or acid treatment, leaving an inverse opal composed of nanoparticles. Nevertheless, the inverse opal is subjected to two fatal problems: the first one is cracking or collapse,^[23–26] which arises from incompact deposition of nanoparticles or inhomogeneous shrinkage of the walls during the template-removing process.^[18,27,28] The second problem is poor electron transport arising from numerous nanoparticles and interfaces in the wall.^[4,18,29] Such structural imperfections usually cause unreliable electrical contact and deteriorate optical and electrical properties.^[27–29]

Many efforts have been made to remedy the above shortcomings. Some works focused on constructing crack-free inverse opals by strengthening template spheres,^[30,31] or adopting carefully designed deposition processes (such as atomic layer deposition,^[32,33] modified chemical vapor deposition.^[34] Other researches worked on improving the electron transport of the inverse opal structures.^[4,18,29,35–41] The popular techniques

involve doping the framework with metal elements (W and Ta),^[40,41] introducing conductive carbon layer,^[4] entrapping conductive nanoparticles,^[35] and coarsening grains in the walls.^[37] Despite of great achievements, there is no report on simultaneously resolving the crack and conductivity problems so far, and it is still a big challenge to develop facile strategies to obtain perfect structure with high conductivity.

CdSe is among the best candidates to construct solar cells because of its direct band-gap, strong absorptivity for sun light, and good electron mobility.^[42–44] Inverse opal structure composed of CdSe nanoparticles is promising for serving as the photoelectrode of solar cells, however, the cracking and poor conductivity must be overcome for its practicability. Being stimulated by steel-reinforced concrete, we propose to introduce one-dimensional nanomaterials with high strength and conductivity into CdSe inverse opal. Carbon nanotubes (CNTs), with a typical Young's modulus of 1 TPa and extension rate up to 30%, are reported to enhance mechanical properties significantly when used as the reinforcement.^[45–47] On the other hand, few-walled carbon nanotubes (FWCNTs), with small number of walls (2–10 layers), can be synthesized more easily than single-walled CNTs, and own lower defect density as well as higher electric conductivity than multi-walled CNTs.^[48–50] Considering their extraordinary mechanical and electrical properties, we utilize FWCNTs to improve simultaneously the strength and the electron transport of CdSe inverse opal. We found that the cracking of inverse opal was depressed remarkably, and the solar cell with CdSe/FWCNTs inverse opal demonstrated power conversion efficiency (PCE) of 1.56%, which is three times of pure CdSe inverse opal (0.53%). The PCE can be further raised to 3.09% by ZnS coating, indicating that FWCNTs-reinforced inverse opal has a bright future for photo-electrical applications.

Figure 1 presents the procedure for the preparation of R-CdSe. First, a conductive glass substrate was inserted vertically into distilled water containing CdSe quantum dots (QDs) with an average size of 3 nm (see Figure S1a, Supporting Information), curly FWCNTs with a diameter of 20 nm (see Figure S1b, Supporting Information), and polystyrene (PS) microspheres of 300 nm in size, as shown in Figure 1a. The FWCNTs displayed a characteristic of n-type conduction according to Hall-effect measurements (Figure S2, Supporting Information), and they were treated with dilute nitric acid in advance to remove catalyst nanoparticles and improve their dispersion in distilled water.^[21] Second, the three component materials deposited together at the substrate–water–air interface which moved downward with continuous evaporation of the liquid. As a result, a PS/FWCNTs/CdSe composite film formed

X.-L. Zheng, Dr. T. Ling, Prof. X.-W. Du
Tianjin Key Laboratory of Composite
and Functional Materials
School of Materials Science and Engineering
Tianjin University
Tianjin 300072, China
E-mail: xwdu@tju.edu.cn

Dr. W.-J. Qin
Institute of Material Physics
Tianjin University of Technology
Tianjin 300384, China

Prof. C.-F. Pan
Beijing Institute of Nanoenergy and Nanosystems
Chinese Academy of Science
Beijing 100083, China

DOI: 10.1002/admi.201400464



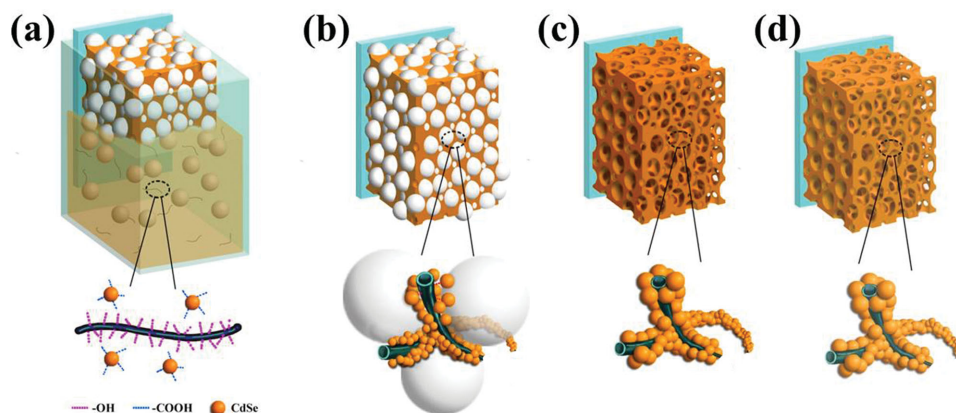


Figure 1. Schematic illustration on the preparation of R-CdSe. a) Co-assembling CdSe QDs, PS spheres, and FWCNTs on the substrate by the evaporation of water. b) The compact film formed on the substrate after co-deposition. c) Formation of R-CdSe by calcination. d) Coating ZnS layer on R-CdSe. The enlarged images at the bottom show the structural details at different stages.

on the substrate (Figure 1b). As the third step, the PS templates were removed via annealing in air at 400 °C for 1 h to yield R-CdSe inverse opal (Figure 1c). The R-CdSe thickness could be easily controlled by adjusting the amounts of PS spheres and CdSe QDs, as shown in Figure S3, Supporting Information. An optimum thickness of 1.4 μm was determined by comparing the photovoltaic performance of samples with different thicknesses (Figure S4 and Table S1, Supporting Information), and further measurements were performed on 1.4 μm-thick R-CdSe. To investigate the effect of FWCNTs, three R-CdSe samples were prepared by using different FWCNTs dosages (50 μL of FWCNTs dispersion for R-CdSe I, 100 μL for R-CdSe II, 150 μL for R-CdSe III, see details in the Experimental Section). Finally, a ZnS layer was coated onto R-CdSe to improve recombination resistance (Figure 1d). As a comparison, P-CdSe was prepared following the same procedure but eliminating FWCNTs in the recipe.

Scanning electron microscope (SEM) images of the as-deposited P-CdSe and R-CdSe II are presented in Figure S5, Supporting Information. The as-deposited P-CdSe shows many cracks even at low magnification, while the as-deposited R-CdSe II looks perfect at the same magnification. The raw CdSe nanoparticles possess a zinc-blend phase structure, which transformed into wurtzite one after being calcinated at 400 °C (Figure S6a, Supporting Information). X-ray photoelectron spectrometer (XPS) survey spectra indicate that the C1s peak of R-CdSe II is higher than that of P-CdSe (Figure S6b, Supporting Information), confirming that the FWCNTs were successfully introduced into R-CdSe.^[51]

After calcination, many huge cracks can be found in sample at the low-magnification SEM image of P-CdSe (Figure 2a), while the R-CdSe sample presents a compact and flat surface in the low-magnification image (Figure 2d). In the high magnification SEM image, the width and length of cracks in P-CdSe are measured as several micrometers and several tens micrometers, respectively (Figure 2b), and the cracks penetrate through the whole depth (Figure 2c). In contrast, no crack is found in the R-CdSe sample (Figure 2e), and the inverse opal structure keeps continuous both in lateral and depth directions (Figure 2f). Moreover, the cross-sectional SEM image

in Figure 2c illustrates that the inverse opal layer detaches away from the fluorine-doped tin oxide (FTO) substrate in the P-CdSe sample, while R-CdSe in Figure 2f demonstrates tight connection with the substrate. In a high-magnification SEM image (Figure 2g), a FWCNT is anchored by two CdSe particles at two ends, and pulled into a straight line, suggesting that FWCNTs can load the stress and play the role of reinforcement. In another high-magnification SEM image, Figure 2h, several CdSe nanoparticles adhere onto a FWCNT tightly, indicating a strong combination between FWCNTs and CdSe nanoparticles. Low-magnification transmission electron microscopy (TEM) image presented in Figure 2i illustrates that a FWCNT keeps the tubular structure and runs through at least four CdSe nanocrystals.

The reinforcement mechanism of FWCNTs can be well understood according to the above results. It was recognized that CdSe QDs synthesized by the present approach are capped with -COOH groups,^[52] while FWCNTs treated by nitric acid possess surface -OH groups,^[53] and the two ligands can react to form a chemical bonding after co-deposition.^[54] During the calcination, PS template, solvent and organic molecules were removed, and the fine nanoparticles in the walls amalgamated and coarsened. All of the changes resulted in a remarkable shrinkage in volume. Such shrinkage causes high internal stress in the walls and then serious breakdown of P-CdSe. In contrast, FWCNTs in R-CdSe can form a tight combination with CdSe crystals (see Figure 2h), thus the stress is transferred efficiently from CdSe nanocrystals to the FWCNTs.^[54] FWCNTs are able to bear the intense stress and depress the volume shrinkage because of their very high strength, which was supposed to be the main reason for inhibiting crack and collapse in R-CdSe effectively. On the other hand, FWCNTs can link a large number of CdSe nanoparticles, enhance their connectivity, and maintain the architecture of the inverse opal.^[55]

Next, we turn to the conductivity properties of the CdSe inverse opal structures. Electrochemical impedance spectroscopy (EIS) analysis was made on different CdSe inverse opals under dark conditions and at different negative biases. Figure 3a displays the results taken at -0.15 V bias, and the inset is the enlargement of the high frequency range of the

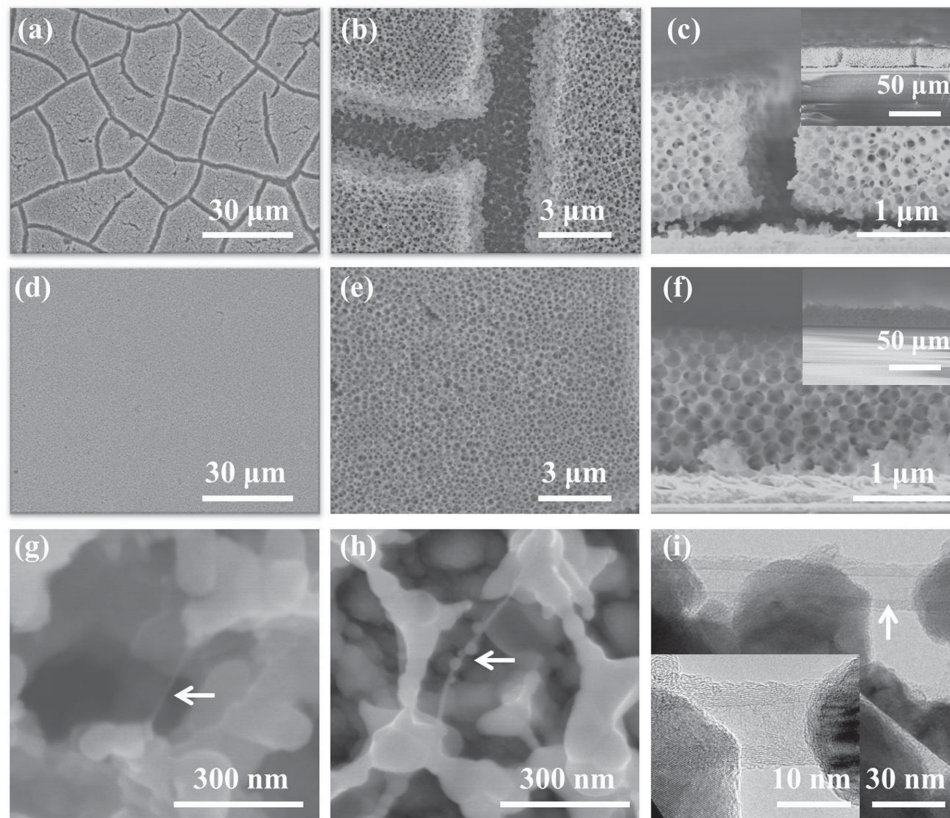


Figure 2. Morphologies of P-CdSe and R-CdSe II after calcination. a–c) are low-magnification plan-view, high-magnification plan-view, and cross-sectional SEM images, respectively, of P-CdSe, the inset in c) is a corresponding low-magnification SEM image. d–f) are low-magnification plan-view, high-magnification plan-view, and cross-sectional SEM images, respectively, of R-CdSe, the inset in f) is a corresponding low-magnification SEM image. g, h) are high magnification SEM images of a FWCNT in CdSe inverse opal. i) Low-magnification TEM image of a FWCNT in CdSe inverse opal, and the inset is the enlarged image on the FWCNT. The arrows in g–i) indicate the FWCNTs.

spectra in panel showing straight lines normally indicative of the Warburg behavior characteristic of a transmission line,^[56–59] correspondingly, a transmission line model developed by Bisquert and co-workers was used to fit the results (Figure 3b). As seen in Figure 3c, P-CdSe structure demonstrated a transport resistance (R_{tr}) value as high as $10^3 \Omega \text{ cm}^2$, which is remarkably reduced after the addition of FWCNTs. Direct voltammetry measurements were also employed to determine the electrical resistance of CdSe inverse opal films (see Figure S7, Supporting Information), the results agree well with the EIS fitting results. Moreover, electron diffusion length (L_n) and electron diffusion coefficient (D_n) can be deduced from the EIS results by $L_n = d\sqrt{R_{ct}/R_{tr}}$ and $D_n = d^2/(R_{tr}C_{\mu})$, respectively, where d is the thickness of the film, R_{ct} the recombination resistance, and C_{μ} the interface capacitance. As presented in Figure 3d,e, L_n and D_n are improved by 4 and 10 times, respectively, by adding 100 μL FWCNTs. These results reveal that the FWCNTs can enhance the electron conductivity of CdSe inverse opal significantly.

To demonstrate the practical application of R-CdSe, we assemble photochemical solar cells with R-CdSe as the photoanode, the cell structure is schematically illustrated in Figure S8, Supporting Information. Figure 4a displays the current density–voltage (J – V) characteristics of the solar cells in the dark. R-CdSe shows lower leakage current than P-CdSe, owing

to the effect of FWCNTs to the intact structure. The dark J – V characteristic of R-CdSe shows the reverse blocking current, while P-CdSe demonstrates symmetrical J – V characteristics. Meanwhile, R-CdSe also displays higher recombination dark current for high surface of CdSe and FWCNTs. Overall, R-CdSe II shows the lowest leakage current and recombination current. Under solar light, the P-CdSe cell is seen to exhibit the lowest short-circuit photocurrent density (J_{SC}), while the J_{SC} values of R-CdSe cells first increase and then decrease with the increase in the concentration of FWCNTs (Figure 4b). R-CdSe II sample achieved the best performance, namely, J_{SC} 9.00 mA cm^{-2} , open circuit voltage (V_{oc}) 0.49 V, and PCE (η) 1.56% (Table 1). The incident photon-to-electron conversion efficiency (IPCE) curves for different samples are shown in Figure 4c. The curve of P-CdSe cell is seen to have a photocurrent onset at 710 nm, and the highest response is obtained at 390 nm. However, all of solar cells display relatively poor response to the visible light, with more noticeable trend over 460 nm. The R-CdSe cells exhibit a similar wavelength-response behaviors with P-CdSe one, but the sensitivity is much higher. Being consistent with the J – V curves, the IPCE values of R-CdSe first increase and then decrease with the μL concentration of FWCNTs, and the sample containing 100 μL FWCNTs exhibits the highest photocurrent generation efficiency, which agrees with the highest J_{SC} value demonstrated by this sample (see Table 1 and Figure 4a).

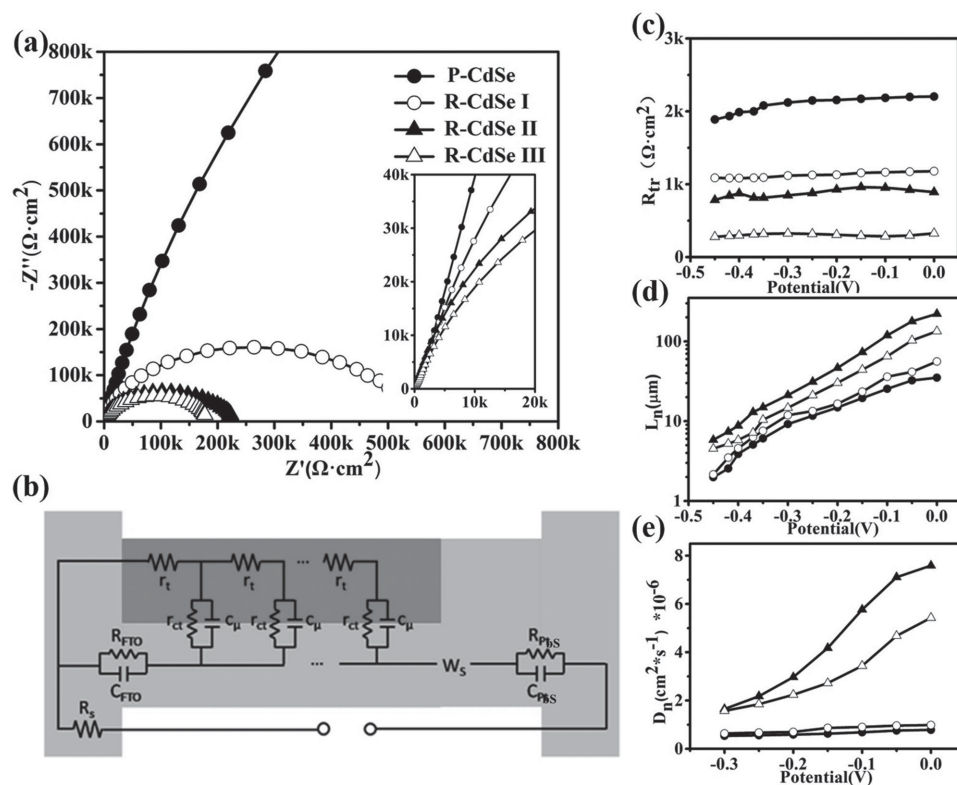


Figure 3. EIS results measured under dark conditions and at different negative-biases. a) EIS spectra of solar cells with different FWCNTs concentrations measured at a bias of -0.15 V, the inset is an enlarged image at high frequency area. b) Equivalent fitting circuit of transmission line model. c) Electron transport resistance (R_{tr}), d) electron diffusion length (L_n), and e) electron diffusion coefficient (D_n) as a function of applied bias voltage.

In order to understand better the performance difference observed in Figure 4, we explore the effect of FWCNTs from the view of energy conversion. **Figure 5a** illustrates the optical absorption properties of CdSe inverse opal with different FWCNTs concentrations. The spectra show absorption onsets around 710 nm, being exactly same with that in IPCE curves. Above results indicate that the photoresponse of solar cells is ascribed to the band gap excitation of CdSe nanocrystals. Moreover, slight increase in absorbance is observed in R-CdSe, which mainly arises from the dark appearance of FWCNTs,^[60] and can contribute partially to the enhanced photocurrent. The excited state transition of CdSe QDs was probed by recording photoluminescence (PL) and time-resolved photoluminescence (TRPL) spectra of CdSe QDs with and without FWCNTs, respectively. As shown in Figure 5b, the addition of FWCNTs quenches the PL of CdSe QDs remarkably. On the other hand, the average lifetime of the CdSe/FWCNTs composite was estimated as 9.89 ns which is much shorter than that of pure CdSe QDs, 36.80 ns (Figure 5c and Table 2). The PL quenching and lifetime reduction hint that the addition of FWCNTs induces a nonradiative de-excitation pathway, namely, electron transfer from the excited CdSe QDs to FWCNTs, as demonstrated in previous studies.^[61,62] Schematic band structure of R-CdSe photoanode along with a SEM cross-sectional image is illustrated in Figure 5d, and the light conversion process can be expressed as following: CdSe nanocrystals are excited by incident light and generated electron-hole pairs (step 1), the electrons in the conductive band transfer to conductive glass through CdSe

skeleton or n-type FWCNTs (step 2). At the same time, the holes in the valence band transfer to the polysulfide electrolyte and the anode (step 3). However, the recombination of electron and holes in CdSe nanocrystals (step 4) or in electrolyte (step 5) can cause dark current and then deteriorate the photo-electron conversion.

To suppress the reverse flow of electrons into the electrolyte and then recombination with holes (step 5), a ZnS layer was coated on the P-CdSe and R-CdSe inverse opal by adopting a successive ion layer adsorption and reaction (SILAR) technique reported in ref. [42], and the SEM and TEM images of R-CdSe with ZnS coating via 3 SILAR cycles are shown in Figure S9, Supporting Information. The effect of FWCNTs and ZnS coating was compared in **Figure 6**. The solar cell with a photoanode of R-CdSe achieves a power conversion efficiency three times of that without FWCNTs. The ZnS coating on the P-CdSe and R-CdSe inverse opal can depress the leaked current efficiently, thus further improve the overall performance of R-CdSe solar cell. The short circuit current density reaches 18 mA cm^{-2} under the illumination of one sun, and the overall conversion efficiency is up to 3.09% (Figure 6 and Table 3).

The PCE improvement in R-CdSe can be understood as below. In case of P-CdSe, the large amount of interfaces and cracks block the electron flow to FTO substrate, thus reducing the short-circuit current. This problem can be well solved by introducing FWCNTs into inverse opals, and the carbon nanotubes function in three ways: (i) Serve as electron acceptor to promote the charge separation and inhibit the electron-hole

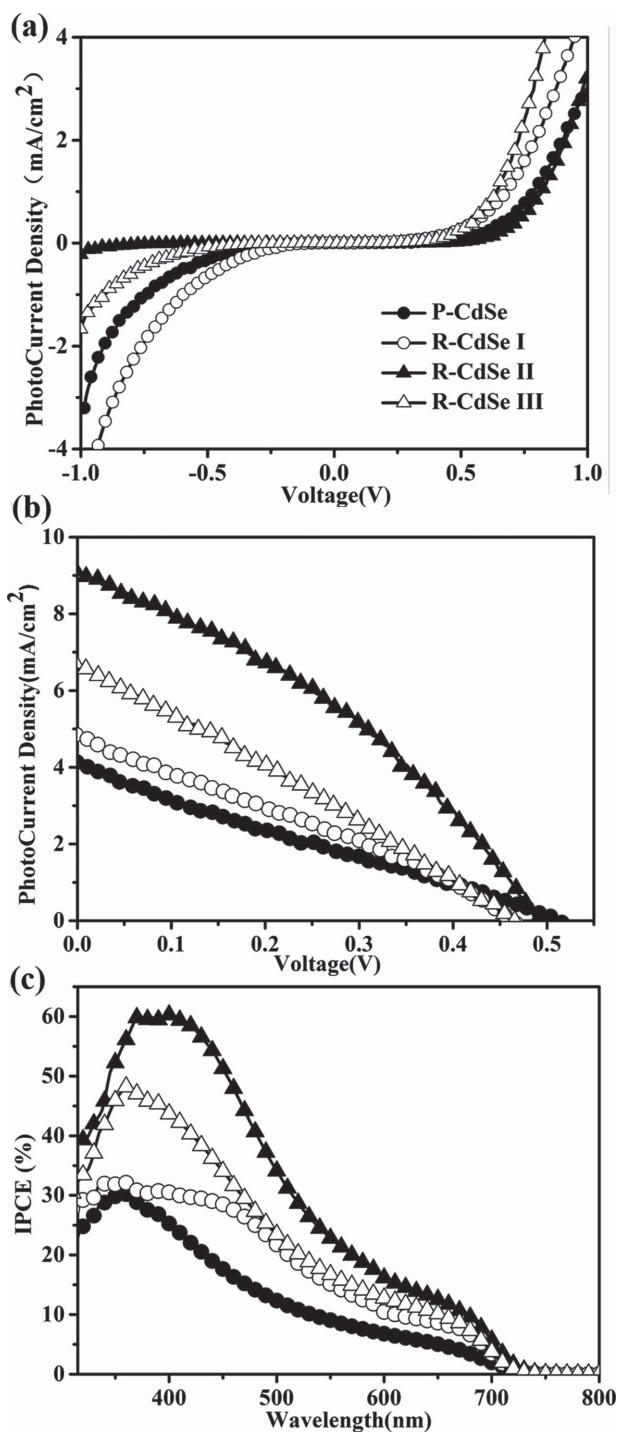


Figure 4. Photoelectric conversion properties of solar cells composed of P-CdSe and R-CdSe. *J*–*V* curves a) in the dark and b) under illumination of one sun (AM1.5, 100 mW cm⁻²), respectively. c) IPCE profiles.

recombination in CdSe; (ii) eliminate cracks and keep intact structure so as to depress the leaked current; (iii) provide a direct channel for electron transfer from CdSe to FTO as a highly conductive additive to shorten the electron transport path. Resultantly, the short-circuit current of R-CdSe cells is remarkably enhanced and the overall PCE is three times that of

Table 1. Experimental result data derived from *J*–*V* profiles in Figure 4.

Sample	CNTs dosage [μL]	V _{OC} [V]	J _{SC} [mA cm ⁻²]	FF [%]	η [%]
P-CdSe	0	0.51	4.22	0.25	0.53
R-CdSe I	50	0.47	4.90	0.27	0.62
R-CdSe II	100	0.50	9.01	0.34	1.53
R-CdSe III	150	0.47	6.64	0.28	0.87

P-CdSe. The ZnS coating on the R-CdSe inverse opal can suppress the reverse flow of electrons into the electrolyte, thus further improve the overall performance of R-CdSe solar cell.

Several works reported on the application of CdSe nanostructures in solar cells as the sole sensitizer.^[42,63] The 3.09% conversion efficiency achieved in this work is the leading value among such solar cells (see Table 4), which can be attributed to successful depression of cracking and improvement on the electron transport, although further clarification is needed for clarifying respective contribution from the two causes.

We introduced FWCNTs into CdSe inverse opal structure to depress the crack and collapse and improve the conductivity simultaneously. FWCNTs connect with CdSe crystals tightly and load the stress efficiently, thus prevent the inverse opal from fracturing. On the other hand, FWCNTs possess fitting energy levels and high conductivity; hence provide a direct channel for electron transfer. The two advantages jointly assist R-CdSe to achieve photo-electrical conversion efficiency two times higher than pure CdSe. The crack-free and highly conductive CdSe inverse opals are of high demand for photovoltaic applications, and they look very promising for the further development of solid-state solar cells.

Experimental Section

Synthesis of Water Stable CdSe Quantum Dots: CdSe QDs were synthesized following a previously reported procedure.^[53] First, 72.73 mg CdCl₂·2.5H₂O and 0.07 mL thioglycolic acid were dissolved in 20 mL deionized water. Then an appropriate dosage of NaOH was added to the mixture until the pH value reached 11.0. The solution was continuously stirred, following by the addition of 75.6 mg NaBH₄ and 12 mg Se powder. Finally, the solution was poured in a 50 mL reaction vessel and reacted for 2.5 h at 96 °C. The precipitated CdSe QDs were separated and redispersed in distilled water, obtained dispersion with a concentration of 3 wt%.

Acid Treatments of FWCNTs: 0.1 g pristine FWCNTs were added to 10.0 mL aqueous HNO₃ with a concentration of 3 M. The mixture was ultrasonically treated for 30 min and then stirred at 80 °C for 24 h. Afterwards, the mixture was vacuum filtered and washed with distilled water until the pH of the filtrate reached 7.0. The product was dried under vacuum for 12 h at 60 °C, and then dispersed in 50 mL distilled water.

Preparation of CdSe Inverse Opal Structures: As-received PS spheres with an average size of 300 nm were dispersed in distilled water and the concentration was adjusted to 6 wt%. 300 μL of PS dispersion, 450 μL of CdSe QDs dispersion, and 50 μL of FWCNTs dispersion were mixed together in a beaker containing 20 mL of distilled water. Then, clean FTO substrates were inserted vertically into the mixture. The beaker was heated in a vacuum oven at 60 °C for 24 h. Upon solvent evaporation, PS spheres, CdSe QDs, and FWCNTs were co-assembled on the FTO

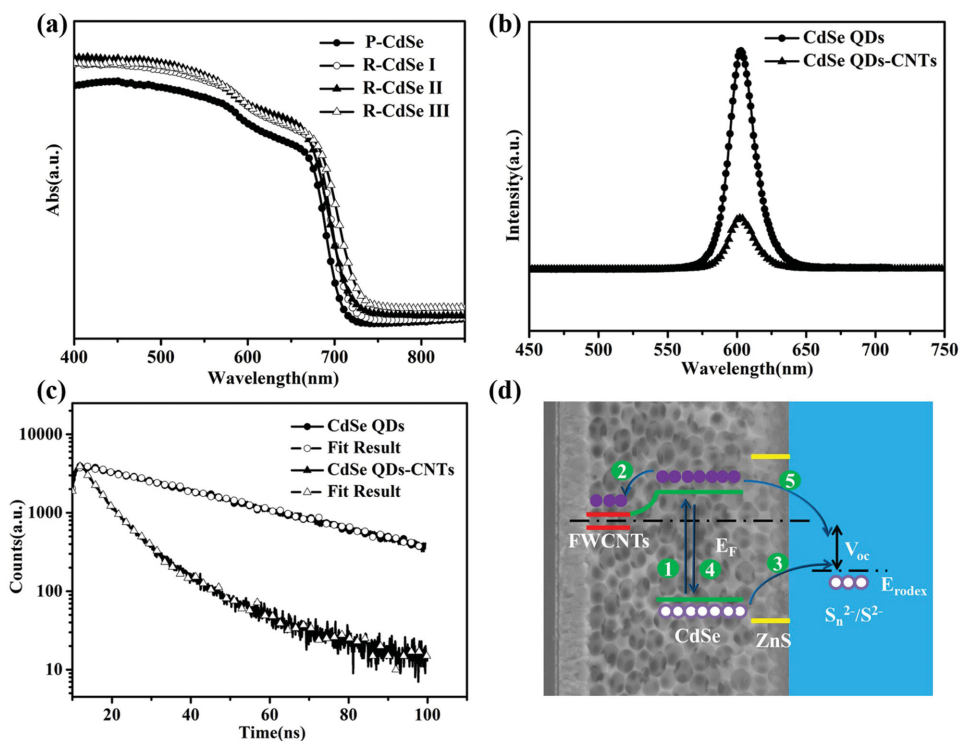


Figure 5. The characterizations of P-CdSe and R-CdSe. a) UV-vis absorption spectra of CdSe inverse opals, b) PL spectra of CdSe QDs with and without FWCNTs under the excitation light of 420 nm, c) TRPL spectra of CdSe QDs with and without FWCNTs recorded at 600 nm excited by a 420 nm laser pulse, d) energy level diagram of the FWCNTs reinforced CdSe inverse opal. E_F is the Fermi level of the CdSe-FWCNTs anode and E_{redox} is the redox potential of electrolyte.

substrates. Finally, the FTO substrates were put in tube furnace, with activated carbon powder placed on both sides to avoid oxidation, heated to 300 °C held the temperature for 1 h to remove PS template, then increased to 400 °C and kept for 1 h to improve the crystallinity of CdSe. As a result, an inverse opal structure named as R-CdSe I was obtained with a thickness around 1.4 μm . Similarly, samples R-CdSe II and R-CdSe III were obtained by using 100 and 150 μL of FWCNTs dispersion but keeping the other parameters constant. To prepare CdSe inverse opals with the thickness of 0.5 and 2.3 μm , the volume of PS dispersion was taken as 107 and 493 μL , respectively, and the volumes of CdSe QDs dispersion were 161 and 740 μL , respectively, while the volumes of FWCNTs dispersion were 36 and 164 μL , respectively. A ZnS layer was coated on the CdSe inverse opal through a SILAR process by immersion in 0.02 M ethanol solution of acetate zinc and 0.02 M aqueous solution of Na_2S alternatively for 3 cycles.^[63] After each cycle, the sample was rinsed with distilled water and dried by air flow. P-CdSe was prepared following the same procedure but eliminating FWCNTs in the recipe.

Solar Cell Assembly: The FTO substrate with CdSe inverse opal and a PbS counter electrode were sealed with a thin transparent hot-melt Surlyn with an active area of 0.24 cm^2 . The PbS counter electrode was prepared following the previously reported procedure.^[64] Polysulfide electrolyte consisting of 0.5 M Na_2S , 2 M S, and 0.2 M KCl in MeOH/ H_2O solvent (volume ratio 7:3) was injected into the inner electrode space from the counter electrode side through a predrilled hole. The

Table 2. Lifetime and amplitude data obtained by fitting the profiles in Figure 5c.

Sample	τ_1 [ns]	$a_1/(a_1+a_2)$ [%]	τ_2 [ns]	$a_2/(a_1+a_2)$ [%]	χ^2	$\langle\tau\rangle$ [ns]
CdSe QDs	36.80	100			1.098	36.80
CdSe QDs-CNTs	5.24	54.42	15.46	45.58	1.068	9.89

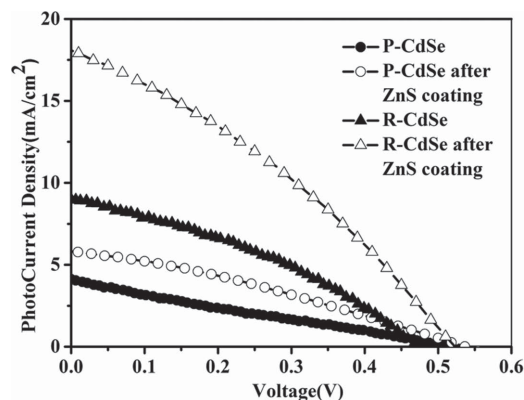


Figure 6. J - V curves of P-CdSe and R-CdSe with and without ZnS coating under illumination of one sun.

schematic presentation of the CdSe inverse opal photoelectrochemical cell is shown in Figure S8, Supporting Information. The active area of the cell was accurately defined by the transparent Surlyn spacer with the

Table 3. Performance of R-CdSe with and without ZnS coating.

Sample	V_{oc} [V]	J_{sc} [mA cm^{-2}]	FF [%]	η [%]
P-CdSe	0.51	4.22	0.25	0.53
P-CdSe with ZnS coating	0.53	5.85	0.33	1.02
R-CdSe II	0.48	9.03	0.34	1.47
R-CdSe II with ZnS coating	0.52	18.00	0.33	3.09

Table 4. Performance characteristics of previously reported different CdSe nanostructures.

CdSe nanostructures	V_{OC} [V]	J_{sc} [mA cm ⁻²]	FF [%]	η [%]	Electrolyte	Reference
CdSe nanoparticle	0.37	12.95	0.26	1.25	Na ₂ S/S	Lai and Chou ^[53]
CdSe nanowires	0.34	2.32	0.58	0.46	Na ₂ S/S	Choi et al. ^[54]
CdSe nanobelt	0.42	13.90	0.32	1.87	Na ₂ S/S	Shi et al. ^[55]
CdSe inverse opal	0.52	18.00	0.33	3.09	Na ₂ S/S	Present work

hollow area of 0.24 cm². A metallic mask with a window of slight larger than 0.24 cm² was clipped on the CdS side to avoid the aperture effect.

Characterization: Morphology observation was performed in a Hitachi S-4800 SEM operated at 5 kV. TEM images are obtained by using an FEI Technai G2 F20 TEM equipped with a field-emission gun operated at 200 kV. x-ray diffraction (XRD) analysis was carried out using a Bruker D/max 2500v/pc diffractometer. XPS data were acquired on a Perkin Elmer 5100 system with a non-monochromatic Al anode X-ray source. The absorption spectra were recorded using a Hitachi 3010 UV-vis absorption spectrometer. PL and TRPL analyses were conducted at room temperature by using an Edinburgh FLS920 fluorescence spectrometer. PL spectra were measured at room temperature with an excitation wavelength of 420 nm, and TRPL profiles were recorded following by a 420 nm laser pulse. J - V curves were measured by a Keithley 2611 digital source meter under an illumination of a solar simulator (Sciencetech, SS150) at one sun (AM 1.5, 100 mW cm⁻²). IPCE spectra were measured with a tungsten quartz halogen light source, mono-chromator, filters, reflective optics to provide monochromatic light, mechanical chopper to modulate the light, and transition impedance amplifier to provide the test device signal to the digital signal processing equipment. EIS data of the cells were collected by using a Versastat 3 Potentiostat-Electrochemistry workstation in the frequency range from 0.1 Hz to 100 kHz under forward bias from 0.00 to -0.45 V. To test the I - V behavior, P-CdSe and R-CdSe films with the thickness of 1.4 μ m were fabricated on glass substrate, and two electrodes were made up of silver paste on each sample with a distance of 20 mm. I - V data were collected in the range from -3 to 3 V at 50 mV s⁻¹ by using the Versastat 3 workstation. The Hall effect measurement was performed in an Accent HL5500 Hall System using four-point van der Pauw-Hall method at room temperature.

Supporting Information

Supporting Information is available from the Wiley Online Library or from the author.

Acknowledgements

This work was supported by The National Basic Research Program of China (Grant No. 2014CB931703), the Natural Science Foundation of China (Grant Nos. 51171127, 51102176, 51271129, and 11272229), Natural Science Foundation of Tianjin City (Grant Nos. 11ZCKFGX01300, 11JCYBJC02000, and 09JCZDJC22600) and Seed Foundation of Tianjin University. The authors declare no competing financial interest.

Received: October 18, 2014

Revised: November 20, 2014

Published online: December 12, 2014

[1] X. S. Zhao, F. Su, Q. Yan, W. Guo, X. Y. Bao, L. Lv, Z. Zhou, *J. Mater. Chem.* **2006**, *16*, 637.

- [2] T. Suezaki, P. G. O'Brien, J. I. Chen, E. Loso, N. P. Kherani, G. A. Ozin, *Adv. Mater.* **2009**, *21*, 559.
- [3] B. T. Holland, *Science* **1998**, *281*, 538.
- [4] A. Esmanski, G. A. Ozin, *Adv. Funct. Mater.* **2009**, *19*, 1999.
- [5] M. Ren, R. Ravikrishna, K. T. Valsaraj, *Environ. Sci. Technol.* **2006**, *40*, 7029.
- [6] J. I. L. Chen, G. von Freymann, S. Y. Choi, V. Kitaev, G. A. Ozin, *J. Mater. Chem.* **2008**, *18*, 369.
- [7] Y.-L. Lee, B.-M. Huang, H.-T. Chien, *Chem. Mater.* **2008**, *20*, 6903.
- [8] S. Guldin, S. Huttner, M. Kolle, M. E. Welland, P. Muller-Buschbaum, R. H. Friend, U. Steiner, N. Tetreault, *Nano Lett.* **2010**, *10*, 2303.
- [9] Y. Chiba, A. Islam, Y. Watanabe, R. Komiya, N. Koide, L. Han, *Jpn. J. Appl. Phys.* **2006**, *45*, L638230L640.
- [10] T. Y. Lee, P. S. Alegaonkar, J.-B. Yoo, *Thin Solid Films* **2007**, *515*, 5131.
- [11] L. Kavan, M. T. Zúkalová, M. Kalbač, M. Graetzel, *J. Electrochem. Soc.* **2004**, *151*, A1301.
- [12] T. P. Hammond, *Adv. Mater.* **2004**, *16*, 1271.
- [13] Y. Li, Z.-Y. Fu, B.-L. Su, *Adv. Funct. Mater.* **2012**, *22*, 4634.
- [14] S. W. Choi, J. Xie, Y. Xia, *Adv. Mater.* **2009**, *21*, 2997.
- [15] J. Lee, S. Shanbhag, N. A. Kotov, *J. Mater. Chem.* **2006**, *16*, 3558.
- [16] Z. Sun, Y. Liu, B. Li, J. Wei, M. Wang, Q. Yue, Y. Deng, S. Kaliaguine, D. Zhao, *ACS Nano* **2013**, *7*, 8706.
- [17] H. He, M. Zhong, D. Konkolewicz, K. Yacatto, T. Rappold, G. Sugar, N. E. David, J. Gelb, N. Kotwal, A. Merkle, K. Matyjaszewski, *Adv. Funct. Mater.* **2013**, *23*, 4720.
- [18] B. Mandlmeier, J. M. Szeifert, D. Fattakhova-Rohlfing, H. Amenitsch, T. Bein, *J. Am. Chem. Soc.* **2011**, *133*, 17274.
- [19] S. Nishimura, N. Abrams, B. A. Lewis, *J. Am. Chem. Soc.* **2003**, *125*, 6306.
- [20] Q. B. Meng, C. H. Fu, Y. Einaga, Z. Z. Gu, A. Fujishima, O. Sato, *Chem. Mater.* **2001**, *14*, 83.
- [21] M. S. Tirumkudulu, *Colloids Surf.* **2005**, *21*, 4938.
- [22] P. V. Braun, P. Wiltzius, *Nature* **1999**, *402*, 603.
- [23] M. Holgado, F. Garcia-Santamaria, A. Blanco, *Colloids Surf.* **1999**, *155*, 4701.
- [24] H. Míguez, F. Meseguer, C. López, Á. Blanco, J. S. Moya, J. Requena, A. Mifsud, V. Fornés, *Adv. Mater.* **1998**, *10*, 480.
- [25] R. G. Shimmin, R. Vajtai, R. W. Siegel, P. V. Braun, *Chem. Mater.* **2007**, *19*, 2102.
- [26] Y. Mi, Y. Chan, D. Trau, P. Huang, E. Chen, *Polymer* **2006**, *47*, 5124.
- [27] Y. Gao, M. Nagai, W.-S. Seo, K. Koumoto, *J. Am. Ceram. Soc.* **2007**, *90*, 831.
- [28] S. Agarwala, M. Kevin, A. S. Wong, C. K. Peh, V. Thavasi, G. W. Ho, *Adv. Colloid Interface Sci.* **2010**, *2*, 1844.
- [29] H. Zhang, P. V. Braun, *Nano Lett.* **2012**, *12*, 2778.
- [30] A. A. Chabanov, Y. Jun, D. J. Norris, *Appl. Phys. Lett.* **2004**, *84*, 3573.
- [31] B. Hatton, L. Mishchenko, S. Davis, K. H. Sandhage, J. Aizenberg, *Proc. Natl. Acad. Sci. U.S.A.* **2010**, *107*, 10354.

- [32] A. Rügge, J. S. Becker, R. G. Gordon, S. H. Tolbert, *Nano Lett.* **2003**, 3, 1293.
- [33] S. C. Riha, B. M. Klahr, E. C. Tyo, S. Seifert, S. Vajda, M. J. Pellin, T. W. Hamann, A. B. F. Martinson, *ACS Nano* **2013**, 7, 2396.
- [34] H. Miguez, N. Tetreault, B. Hatton, S. M. Yang, D. Perovic, G. A. Ozin, *Chem. Commun.* **2002**, 32, 2736.
- [35] X. Huang, J. Chen, Z. Lu, H. Yu, Q. Yan, H. H. Hng, *Sci. Report.* **2013**, 3, 435.
- [36] H. N. Kim, H. Yoo, J. H. Moon, *Nanoscale* **2013**, 5, 4200.
- [37] T. Ling, S. A. Kulinich, Z.-L. Zhu, S.-Z. Qiao, X.-W. Du, *Adv. Funct. Mater.* **2013**, 2, 232.
- [38] J. Ma, B. R. Parajuli, M. G. Ghossoub, A. Mihi, J. Sadhu, P. V. Braun, S. Sinha, *Nano Lett.* **2013**, 13, 618.
- [39] Q. Zhong, H. Xu, H. Ding, L. Bai, Z. Mu, Z. Xie, Y. Zhao, Z. Gu, *Colloids Surf. A* **2013**, 433, 59.
- [40] C. V. Subban, I. C. Smith, F. J. Disalvo, *Small* **2012**, 8, 2824.
- [41] J.-H. Choi, S.-H. Kwon, Y.-K. Jeong, I. Kim, K.-H. Kim, *J. Electrochem. Soc.* **2011**, 158, B749.
- [42] H. Choi, M. Kuno, G. V. Hartland, P. V. Kamat, *J. Mater. Chem. A* **2013**, 1, 5487.
- [43] I. J. Kramer, E. H. Sargent, *Chem. Rev.* **2013**, 114, 863.
- [44] Z. Pan, H. Zhang, K. Cheng, X. H. Zhong, *ACS Nano* **2012**, 6, 3982.
- [45] A. Dillon, *Chem. Rev.* **2010**, 110, 6856.
- [46] Q. Cao, H. S. Kim, N. Pimparkar, J. P. Kulkarni, C. Wang, M. Shim, K. Roy, M. A. Alam, J. A. Rogers, *Nature* **2008**, 454, 495.
- [47] Q. Zheng, Q. Xue, K. Yan, X. Gao, Q. Li, L. Hao, *Polymer* **2008**, 49, 800.
- [48] H.-D. Jeong, J.-H. Lee, B.-G. Lee, H.-J. Jeong, G.-W. Lee, D.-S. Bang, D.-H. Cho, Y.-B. Park, K.-H. Jhee, *Carbon Lett.* **2011**, 12, 207.
- [49] Y. Hou, J. Tang, H. Zhang, C. Qian, Y. Feng, J. Liu, *ACS Nano* **2009**, 3, 1057.
- [50] W. Liedtke, M. Yeo, H. Zhang, Y. Wang, M. Gignac, S. Miller, K. Berglund, J. Liu, *Small* **2013**, 9, 1066.
- [51] J. Du, X. Lai, N. Yang, J. Zhai, D. Kisailus, F. Su, D. Wang, L. Jiang, *ACS Nano* **2010**, 5, 590.
- [52] Y. Wang, J. P. Lu, Z. F. Tong, *Bull. Mater. Sci.* **2010**, 33, 543.
- [53] R. H. Bradley, K. Cassity, R. Andrewsc, M. Meierc, S. Osbeckd, A. Andreud, C. Johnstona, A. Crossley, *Appl. Surf. Sci.* **2012**, 258, 4835.
- [54] I. Robel, M. K. Subramanian, *J. Am. Chem. Soc.* **2006**, 128, 2385.
- [55] E. Shi, X. Qin, Z. Li, L. Zhang, Z. Li, P. Li, Y. Jia, C. Ji, J. Wei, K. Wang, H. Zhu, D. Wu, Y. Li, Y. Fang, W. Qian, F. Wei, A. Cao, *Energ. Environ. Sci.* **2012**, 5, 6119.
- [56] J. Kim, H. Choi, C. Nahm, J. Moon, C. Kim, S. Nam, D.-R. Jung, B. Park, *J. Power Sources* **2011**, 196, 10526.
- [57] J. Song, G. R. Li, F. Y. Xiong, X. P. Gao, *J. Mater. Chem.* **2012**, 22, 20580.
- [58] C. He, Z. Zheng, H. Tang, L. Zhao, F. Lu, *J. Phys. Chem. C* **2009**, 113, 10322.
- [59] F. Fabregat-Santiago, G. Garcia-Belmonte, I. Mora-Sero, J. Bisquert, *Phys. Chem. Chem. Phys.* **2011**, 13, 9083.
- [60] L. J. Brennan, M. T. Byrne, M. Bari, Y. K. Gun'ko, *Adv. Energy. Mater.* **2011**, 1, 472.
- [61] J. H. Bang, P. V. Kamat, *ACS Nano* **2011**, 5, 9421.
- [62] D. M. Guldi, G. A. Rahman, V. Sgobba, N. A. Kotov, D. Bonifazi, M. Prato, *J. Am. Chem. Soc.* **2006**, 128, 2315.
- [63] C. H. Lai, P. T. Chou, *Chem. Commun.* **2011**, 47, 3448.
- [64] Z. Tachan, M. Shalom, I. Hod, S. Rühle, S. Tirosh, A. Zaban, *J. Phys. Chem. C* **2011**, 115, 6162.